Supplementary information for

Tunable Dirac Fermion Dynamics in Topological Insulators

Chaoyu Chen[1], Zhuojin Xie[1], Ya Feng[1], Hemian Yi[1], Aiji Liang[1], Shaolong He[1], Daixiang Mou[1], Junfeng He[1], Yingying Peng[1], Xu Liu[1], Yan Liu[1], Lin Zhao[1], Guodong Liu[1], Xiaoli Dong[1], Jun Zhang[1], Li Yu[1], Xiaoyang Wang[2], Qinjun Peng[2], Zhimin Wang[2], Shenjin Zhang[2], Feng Yang[2], Chuangtian Chen[2], Zuyan Xu[2] and X. J. Zhou[1,*]

[1] *Beijing National Laboratory for Condensed Matter Physics, Institute of Physics, Chinese Academy of Sciences, Beijing 100190, China*

[2] *Technical Institute of Physics and Chemistry, Chinese Academy of Sciences, Beijing 100190, China.*

[*] *Corresponding author: XJZhou@aphy.iphy.ac.cn.*

(Dated: March 1, 2013)

1 Crystal growth and characterization.

The crystal structure of $Bi_2(Te,Se)_3$ is rhombohedral with the space group D_{3d}^5 ($R\overline{3}m$) containing five atoms in the unit cell. The material consists of five-atom layers arranged along the z-direction, known as quintuple layers. In Fig. S1a, crystal structure of $Bi_2(Te_1Se_2)$ is illustrated. Each quintuple layer consists of five atoms, with two equivalent Se atoms, two equivalent Bi atoms and one Te atom. The $\overrightarrow{c}$ axis in Fig. S1a represents the trigonal axis (three-fold rotation symmetry) along z-direction, $\overrightarrow{b}$ axis represents the binary axis (two-fold rotation symmetry) along the x-direction and $\overrightarrow{a} + \frac{\mathbf{1}}{\mathbf{2}}\overrightarrow{b}$ axis represents the bisectrix axis (in the reflection plane) along the y-axis.

High quality single crystals of $Bi_2(Te_{3-x}Se_x)$ ($0 \leq x \leq 3$) were grown by the self-flux method. Bismuth, selenium and tellurium powders were weighed according to the stoichiometric $Bi_2(Te_{3-x}Se_x)$ composition. After mixing thoroughly, the powder was loaded in alumina crucible and sealed in a quartz tube. The above processes were all done in an argon-atmosphere glove box with $O_2 \leq 0.1\ ppm$ and $H_2O \leq 0.1\ ppm$. The quartz tubes were took out and sealed after being evacuated. The mixed materials were heated to 1000 °C, held for 12 hours to obtain a high degree of mixing, and then slowly cooled down to 500 °C over 100 hours before cooling to room temperature. Single crystals of nearly one centimeter in size were obtained by cleaving. The resulting Bi_2Te_3 crystals are hole-doped (p-type). For the growth of n-type Bi_2Te_3, slight excess tellurium was used in the starting composition.

Single crystal of Bi_2Se_3 can also be grown in a four-mirror optical floating zone furnace in the traveling solvent zone configuration. The mixed powder was placed in a quartz tube which is 5 mm in inner diameter and 15 cm in length. After being pre-melted in a vertical furnace, the quartz tube was then suspended from the upper shaft of the floating zone furnace. The pre-melted material was melted by focused radiation heating from four 300 W halogen lamps. Crystal growth process was performed by moving the mirror stage from the bottom of the quartz tube to the top with growth rate 5 $mm/hour$. Because of more stable growth condition, all the powder sealed in the quartz tube formed an entire piece of single crystal from which pieces of several centimeters in size can be cleaved out.

The crystal structure was examined by use of a rotating anode x-ray diffractometer with Cu K_α radiation ($\lambda = 1.5418$ Å). Single crystal X-ray diffraction patterns of $Bi_2(Te_{3-x}Se_x)$ with 7 different compositions were shown in Fig. S1b. Each peak in the diffraction pattern

can be indexed to the hexagonal lattice. Lattice constant, **c**, representing the height of the hexagonal unit cell, derived from the patterns, is shown in Fig. S1c. As expected, it shows a linear dependence on selenium content x in $Bi_2(Te_{3-x}Se_x)$.

The peak width in the X-ray diffraction pattern is a good measure of crystal quality so we have analyzed the peak width in the X-ray diffraction data. As shown in Fig. S1e, the (0 0 15) diffraction peak of the p-type Bi_2Te_3 is fitted with a Lorentzian lineshape which gives a narrow peak width of 0.0718^o (Full Width at Half Maximum, FWHM), indicating the high quality of crystallinity for this sample. In Fig. S1f, the (0 0 15) peak width shows little variation with the selenium content, x, in $Bi_2(Te_{3-x}Se_x)$, suggesting a comparable quality of these samples.

The chemical composition of the crystals was analyzed by induction-coupled plasma atomic emission spectroscopy (ICP-AES), as shown in Fig. S1d. The measured composition of the crystals basically follows the nominal composition.

2 Laser-ARPES measurements.

The angle-resolved photoemission measurements were carried out on our vacuum ultraviolet (VUV) laser-based angle-resolved photoemission system. The photon energy of the laser is 6.994 eV with a bandwidth of 0.26 meV. The energy resolution of the electron energy analyzer (Scienta R4000) is set at 1 meV, giving rise to an overall energy resolution of ∼1 meV which is significantly improved from 10∼15 meV of regular synchrotron radiation-based ARPES measurements on topological insulators. The momentum resolution is $\sim 0.004\ \mathring{A}^{-1}$ for 30^o angular mode and $\sim 0.002\ \mathring{A}^{-1}$ for 14^o angular mode of the R4000 electron energy analyzer. The 30^o angular mode has $\sim \pm\ 0.2\ \mathring{A}^{-1}$ momentum coverage at the center of surface Brillouin zone (Fig. S2a) while the 14^o angular mode covers $\sim \pm\ 0.1\ \mathring{A}^{-1}$ momentum space(Fig. S2b). For p-type Bi_2Te_3, we used 14^o angualr mode for a higher momentum resolution while for other samples the 30^o angualr mode is used as the momentum space occupied by surface states is larger. The superior instrumental resolution of our laser ARPES has made the measured features of topological insulators much sharper, as seen from the measured band structures shown in the right panels of Fig. S2a and Fig. S2b. The Fermi level is referenced by measuring on a clean polycrystalline gold that is electrically connected to the sample. The samples were all cleaved and measured in vacuum with a base pressure better than 5×10^{-11} Torr and a temperature T $\sim 20\ K$.

3 Effect of background substraction on the MDC fitting.

For $Bi_2(Te_{3-x}Se_x)$ with $1.5 \leq x \leq 3$, the bulk conduction continuum coexists with surface states, resulting in a non-standard Lorentzian line-shape for MDCs at the Fermi level. To fit the surface state MDCs with Lorentzian line-shape, two different kinds of background (a constant background and a parabola background) were used. By approximating the bulk conduction continuum as a parabola, MDCs at the Fermi level were well fitted by two Lorentzian peaks, as shown in Fig. S3b. The fitted MDC width (full width at half maximum, FWHM) and the peak position are shown in Fig. S3c. It is noted that, even by using a constant background, the obtained results are similar that have little effect on the main characteristics like the "kink" in dispersion and the "drop" in the MDC width.

4 MDC width and electron mobility.

Fig. S4 shows typical MDCs for p-type Bi_2Te_3, $Bi_2(Te_{2.75}Se_{0.15})$ and Bi_2Se_3 at the Fermi level and at another higher binding energy. The fitted MDC width for the p-type Bi_2Te_3 along $\overline{\Gamma}$ – $\overline{K}$ direction is $\Delta k \sim 0.004\mathring{A}^{-1}$(right panel of Fig. S4a). To the best of our knowledge, this is the sharpest MDC width observed so far by ARPES on topological insulators. The electron mobility $\mu^{'}$ can be estimated from $\mu^{'} = e\ell^{'}/(\hbar k_F)$ with $\ell^{'}$ being the electron mean free path and k_F being the Fermi momentum. For the p-type Bi_2Te_3, $\ell^{'} = 1/\Delta k = 250\mathring{A}$ and $k_F = 0.035\mathring{A}^{-1}$, leading to $\mu^{'} = 1084\ cm^2V^{-1}s^{-1}$. For $Bi_2(Te_{2.75}Se_{0.15})$ and Bi_2Se_3, the electron mobility is calculated to be 96 $cm^2V^{-1}s^{-1}$ and 68 $cm^2V^{-1}s^{-1}$, respectively.

5 Effect of band warping on electron-phonon coupling.

In some samples like $Bi_2(Te_{2.75}Se_{0.15})$, while the surface state dispersion along the $\overline{\Gamma}$ – $\overline{K}$ direction is almost linear (Fig. S5a) and clear signatures of electron-phonon coupling, such as a peak in the real part and a drop in the imaginary part of the electron self-energy can be observed (Fig. S5b and c), the dispersion along the $\overline{\Gamma}$ – $\overline{M}$ direction (Fig. S5d) shows a clear band warping that complicates the analysis of the electron-phonon coupling. The identification of the electron-phonon coupling in these samples are based on several observations. First, band warping usually gives a smooth change in the band and the MDC width, while electron-phonon coupling gives an abrupt change at the characteristic energy scale. Second, the electron-phonon coupling causes a drop in the imaginary part of the electron self-energy below the characteristic energy scale. This is contrary to the band width

broadening shown in Fig. S5e. Third, we can still resolve the signature of electron-phon coupling on top of the band warping effect. In Fig. S5e, the electron-phonon coupling-induced structure, as a cusp near 15 meV binding energy, can still be discerned. For the real part of the electron self-energy, despite the big hump caused by the band warping effect, a signature of the electron-phonon coupling (as indicated by arrow) is visible when examined in a relatively small energy region (Fig. S5f and the inset). For comparison between different samples as in Fig. 3 in the main text, we chose the measurements along the $\overline{\Gamma} - \overline{K}$ direction that give an nearly linear dispersion.

6 Evolution of Fermi surface with composition, x, in $Bi_2(Te_{3-x}Se_x)$.

The evolution of Fermi surface with the composition x in $Bi_2(Te_{3-x}Se_x)$ are shown in Fig. S6; the corresponding band structures are shown in Fig. 3 in the main text. For the p-type Bi_2Te_3 (Fig. S6a1) and $Bi_2(Te_{2.95}Se_{0.05})$ (Fig. S6a2), the surface state coexists with the bulk valence band state. For $Bi_2(Te_{3-x}Se_x)$ with $0.15 \leq x < 1.5$ (Fig. S6a3 to b3), in spite of the dramatic shape change, the Fermi surface consists of surface state only. For $Bi_2(Te_{3-x}Se_x)$ with $1.5 \leq x \leq 3$ (Fig. S6b4 to Fig. S6c4), the surface state coexists with the bulk conduction band state and the samples become n-type.

7 Raman scattering spectra of $Bi_2(Te_{3-x}Se_x)$.

Raman scattering spectra of p-type Bi_2Te_3, $Bi_2(Te_{2.0}Se_{1.0})$, $Bi_2(Te_{1.0}Se_{2.0})$, Bi_2Se_3 and n-type Bi_2Te_3 were obtained by use of a JY HR800 Raman spectrometer with $\lambda = 532$ nm laser. With increasing x in $Bi_2Te_{3-x}Se_x$, the phonon peaks shift to higher energy. The frequency of the A_{1g}^2 mode shifts from 135 cm^{-1} for Bi_2Te_3 to 174 cm^{-1} for Bi_2Se_3. Although the electron-phonon coupling strength is different for p-type and n-type Bi_2Te_3, their phonon frequencies are similar in the measured Raman spectra.

8 Temperature dependence of electron-phonon coupling in $Bi_2(Te_{1.5}Se_{1.5})$.

In Fig. S8, the temperature dependence of the Dirac fermion self-energy in $Bi_2(Te_{1.5}Se_{1.5})$ is shown. The electron-phonon coupling signature, namely, the peak in the real part of the self-energy persists up to 100 K and becomes invisible at 150 K. The electron-phonon coupling strength, defined by the slope of the real part of the self-energy at the Fermi level, decreases with the increasing temperature.

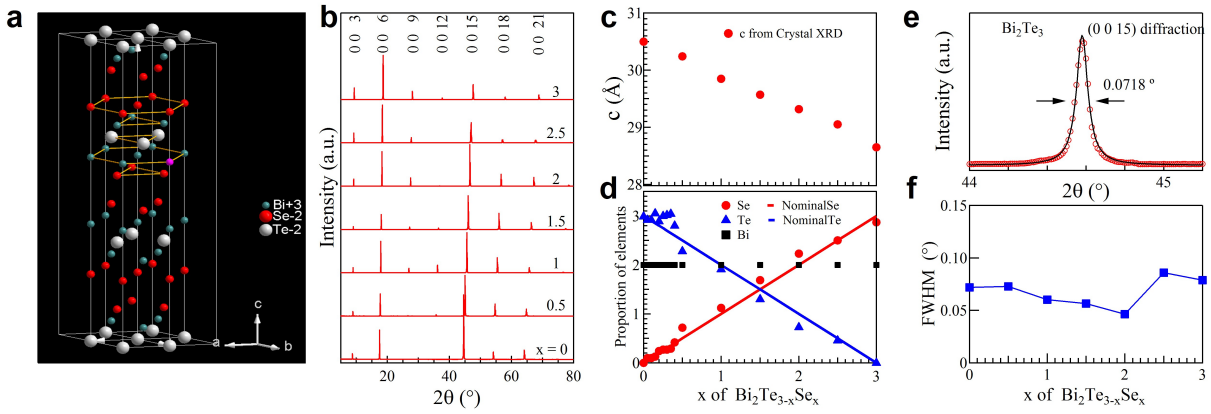

FIG. S1: Characterization of $Bi_2(Te_{3-x}Se_x)$ ($0 \leq x \leq 3$) single crystals. (a) Crystal structure of $Bi_2(Te_1Se_2)$. (b) Single crystal X-ray diffraction patterns of $Bi_2(Te_{3-x}Se_x)$ for x = 0, 0.5, 1.0, 1.5, 2.0, 2.5 and 3. (c) Hexagonal lattice constant **c** derived from the diffraction patterns. (d) Element ratios from the ICP-AES analysis. We set the composition of Bi (black squares) as 2 for normalization. Red dots indicate Se ratio while the red line shows the nominal Se composition. Similarly, blue triangles represent measured Te composition while the blue line shows the nominal composition. (e) Full width at half maximum (FWHM) of the (0 0 15) diffraction peak for the p-type Bi_2Te_3 (red circles) with Lorentzian lineshape fitting (black line). (f) Selenium composition (x) dependence of the peak width in the $Bi_2(Te_{3-x}Se_x)$ samples.

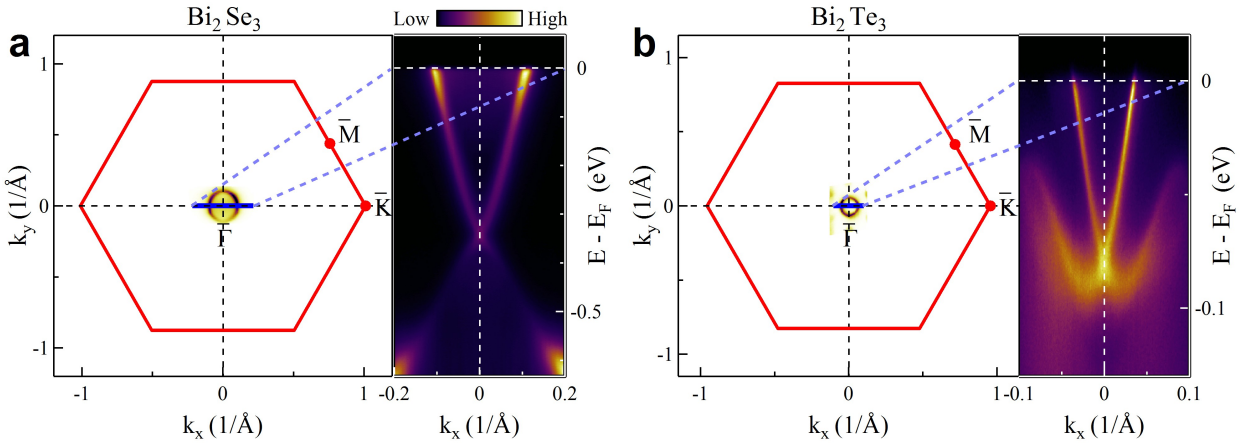

FIG. S2: Momentum coverage for different angular modes of our Scienta R4000 electron energy analyzer. (a) For Bi_2Se_3, blue line indicates one "cut" across $\overline{\Gamma}$ point of surface Brillouin zone and its length represents the momentum coverage($\sim \pm 0.2\ \mathring{A}^{-1}$) for the 30^o angular mode at a photon energy of 6.994 eV. The corresponding band structure measured along $\overline{\Gamma}$ – $\overline{K}$ direction from this "cut" is shown in the right panel. (b) The momentum coverage for the 14^o angular mode and the band structure measured from the $\overline{\Gamma}$ point-crossing "cut" of p-type Bi_2Te_3.

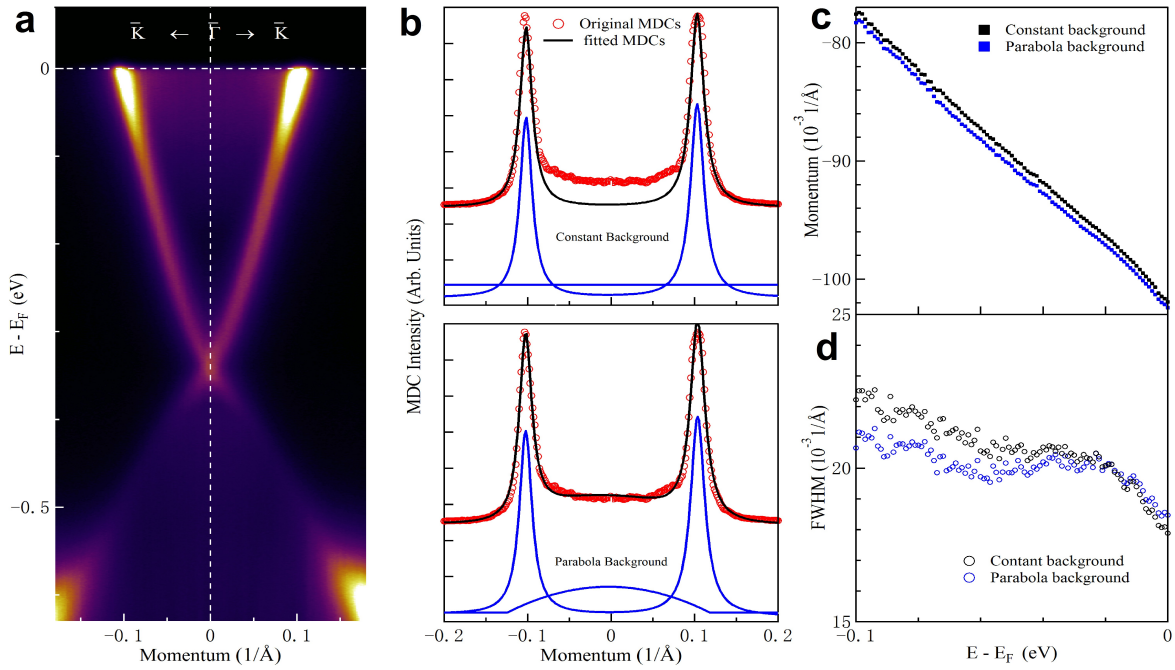

FIG. S3: MDC fitting to two Lorentzian peaks with different kinds of background. (a) Band structure of Bi_2Se_3 measured along the $\overline{\Gamma} - \overline{K}$ direction. The MDC at the Fermi level is used in the curve fitting. (b) MDC fitting results using two Lorentzian peaks with a constant background (top panel) and a parabola background (bottom panel). Red circles are original MDCs and black lines are fitted results. Blue lines represent the fitted Lorentzian peaks and corresponding backgrounds. (c, d) The fitted peak positions (c) and MDC width (d) using different backgrounds.

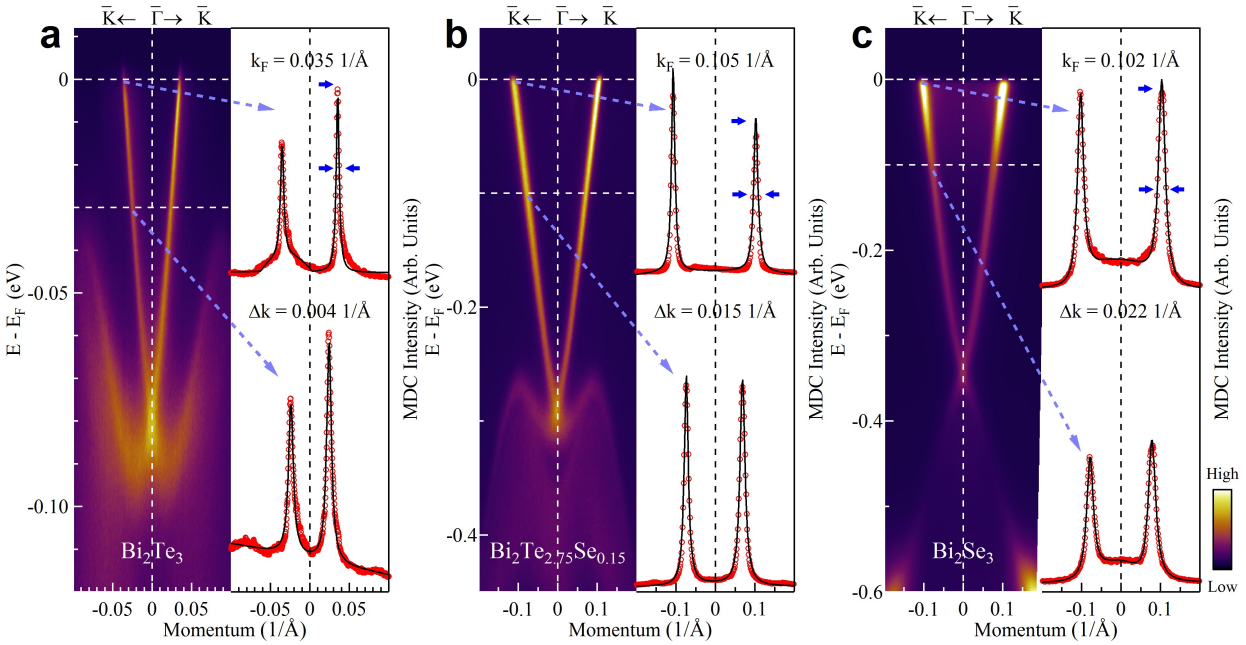

FIG. S4: MDC fitting results of the surface state measured along the $\overline{\Gamma}$ – $\overline{K}$ direction. (a) The measured band structure of p-type Bi_2Te_3 (left panel) and its corresponding MDC fitting (Right panel). The MDCs at the Fermi level and at 30 meV binding energy are used as examples. (b) and (c) show data of $Bi_2(Te_{2.75}Se_{0.15})$ and Bi_2Se_3, respectively, and the MDCs are from the binding energies of 0 meV and 100 meV.

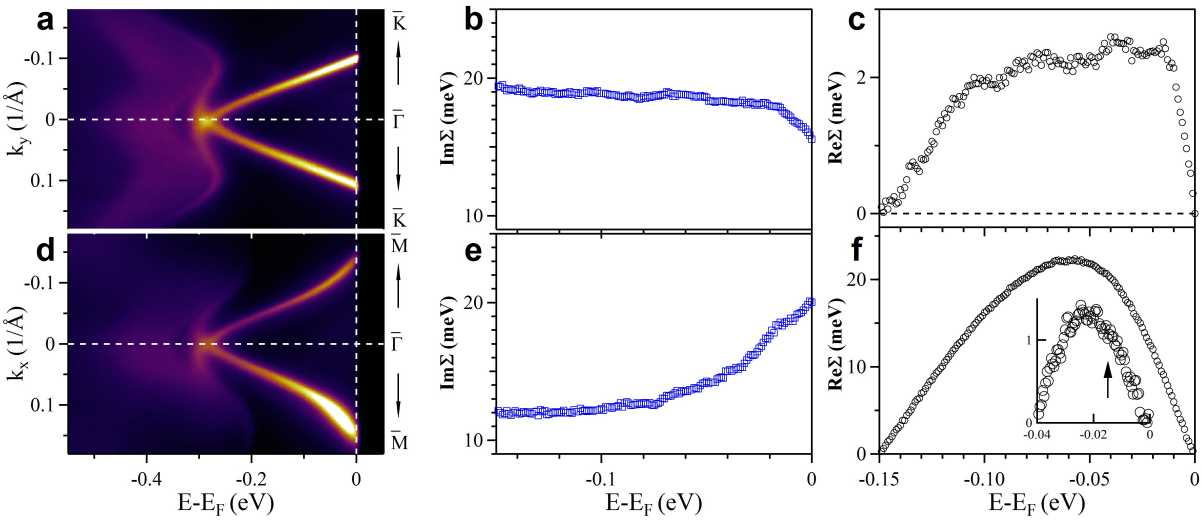

FIG. S5: Effect of band warping on the electron-phonon coupling identification in $Bi_2(Te_{2.75}Se_{0.15})$. (a) Surface state band structure measured along the $\overline{\Gamma}$ – $\overline{K}$ direction. (b, c) Imaginary and real parts of electron self-energy along $\overline{\Gamma}$ – $\overline{K}$ direction show signature of electron-phonon coupling. (d to f) Surface states along $\overline{\Gamma}$ – $\overline{M}$ direction show both signatures caused by band warping effect and the electron-phonon coupling.

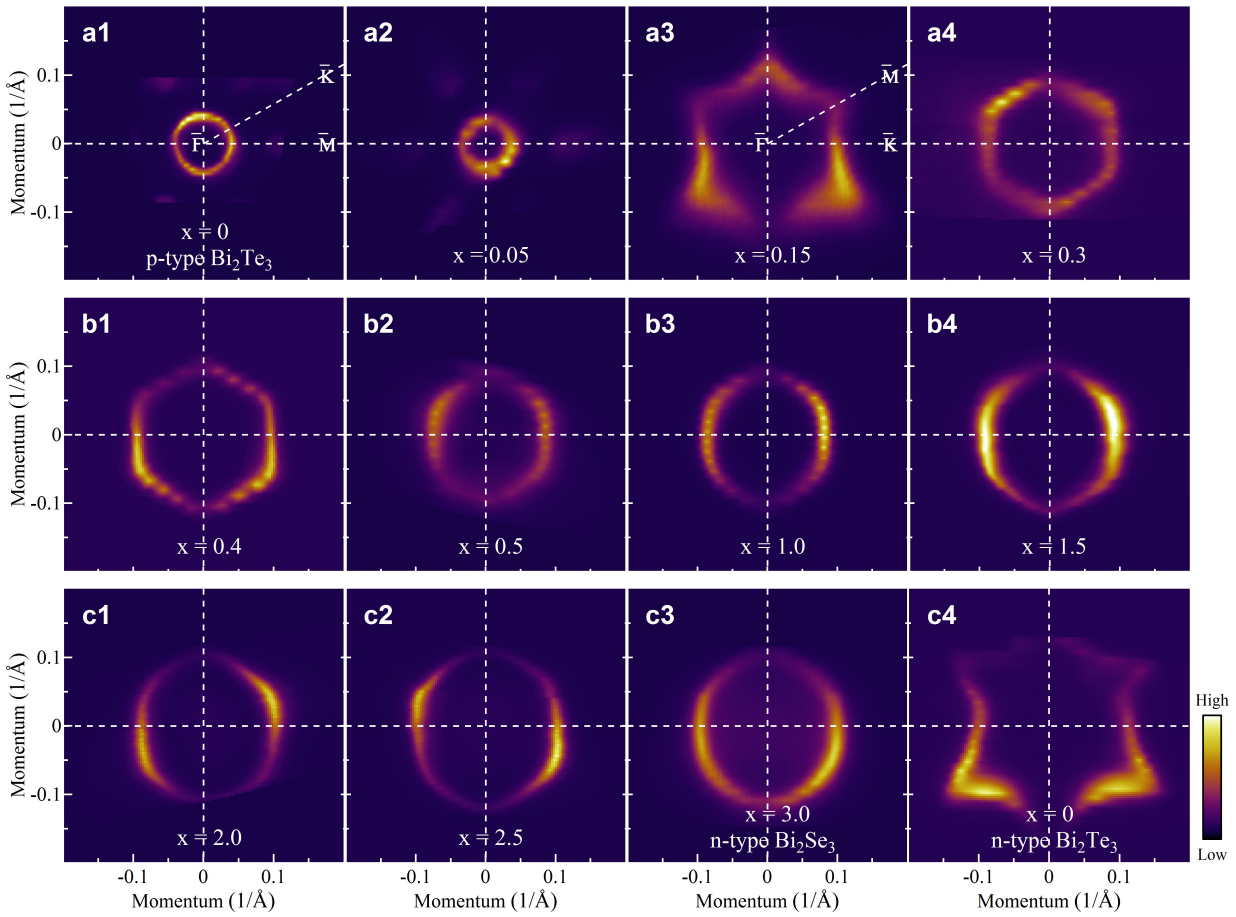

FIG. S6: Fermi surface of $Bi_2(Te_{3-x}Se_x)$. (a1, a2) For p-type Bi_2Te_3 and $Bi_2(Te_{2.95}Se_{0.05})$, the surface state Fermi surface is nearly circular, accompanied by the appearance of six petal-like bulk Fermi surface sheets. (a3) For $Bi_2(Te_{2.85}Se_{0.15})$, the Fermi surface is hexagram-like. (a4, b1) For $Bi_2(Te_{2.7}Se_{0.3})$ and $Bi_2(Te_{2.6}Se_{0.4})$, Fermi surfaces are nearly perfect hexagon. (b2 to b4) For $Bi_2(Te_{2.5}Se_{0.5})$, $Bi_2(Te_2Se_1)$ and $Bi_2(Te_{1.5}Se_{1.5})$, the Fermi surfaces are circular. (c1 to c3) For $Bi_2(Te_1Se_2)$, $Bi_2(Te_{0.5}Se_{2.5})$ and Bi_2Se_3, the Fermi surfaces are circular with hexagonal characteristics. (c4) For n-type Bi_2Te_3, the Fermi surface is hexagram.

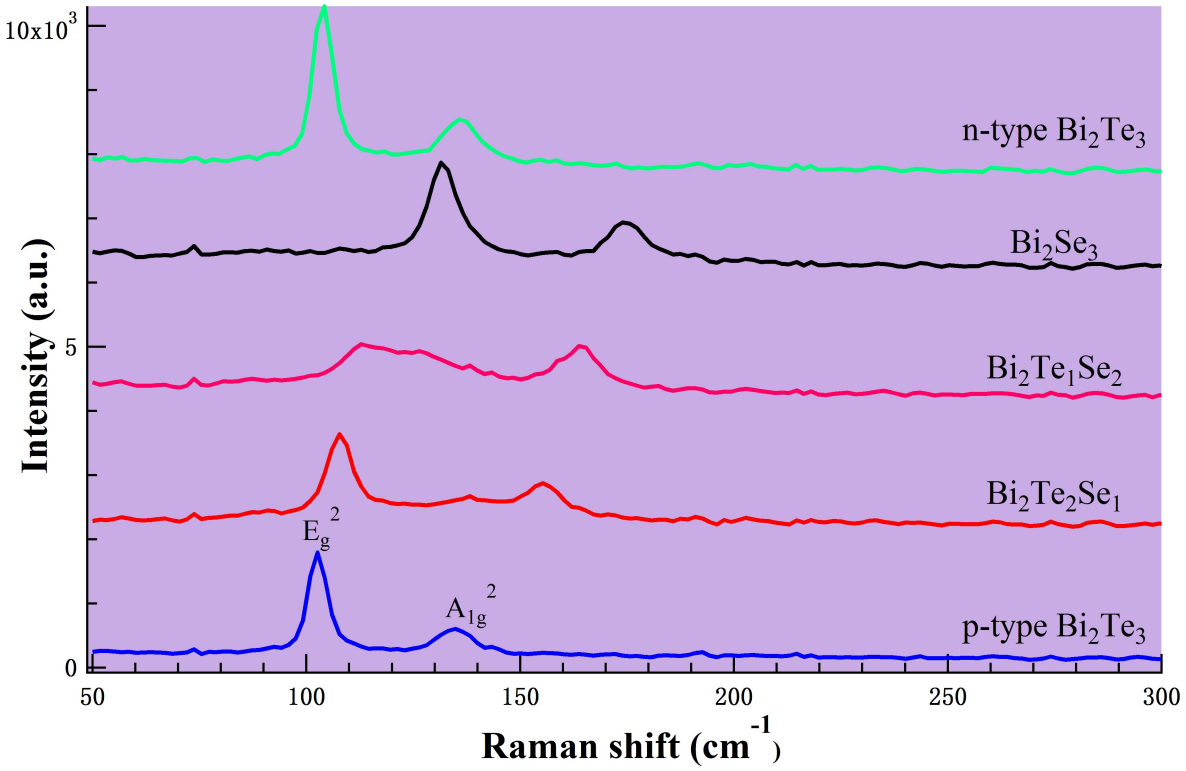

FIG. S7: Raman scattering spectra of $Bi_2(Te_{3-x}Se_x)$. Two vibration modes, E_g^2 and A_{1g}^2, are observed in these samples.

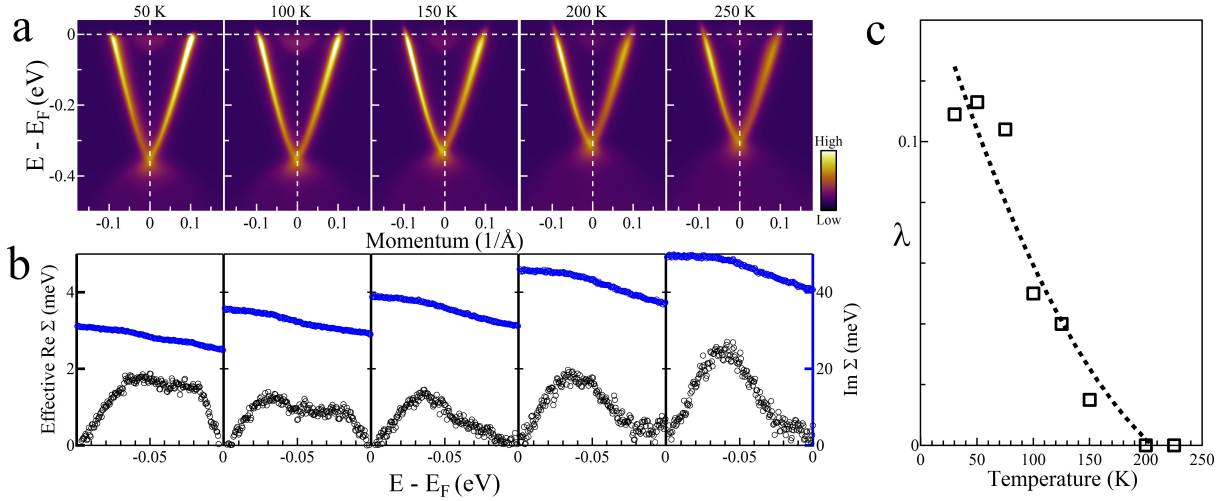

FIG. S8: Temperature dependent self-energy of $Bi_2(Te_{1.5}Se_{1.5})$.(a) Surface state band structure measured along the $\overline{\Gamma} - \overline{K}$ direction at different temperatures. (b) The real part of the electron self-energy (black circles) and the imaginary part of the electron self-energy (blue circles) at different temperatures corresponding to dispersions in (a). (c) Temperature dependence of the electron-phonon coupling strength λ obtained from the real part of the electron self-energy.